# Modeling the effects of active wake mixing on wake behavior through large scale coherent structures

Lawrence Cheung[1], Gopal Yalla[2], Prakash Mohan[3], Alan Hsieh[2], Kenneth Brown[2], Nathaniel deVelder[2], Daniel Houck[2], and Marc T. Henry de Frahan[3]

[1]Sandia National Laboratories, Livermore, CA
[2]Sandia National Laboratories, Albuquerque, NM
[3]National Renewable Energy Laboratory, Golden, CO

**Correspondence:** Lawrence Cheung (lcheung@sandia.gov)

**Abstract.** The use of active wake mixing (AWM) to mitigate downstream turbine wakes has created new opportunities for reducing power losses in wind farms. However, many current analytical or semi-empirical wake models do not capture the flow instabilities which are excited through the blade pitch actuation. In this work, we develop a framework for modeling AWM which accounts for the impacts of the large-scale coherent structures and turbulence on the mean flow. The framework uses
5 a triple-decomposition approach for the unsteady flow field, and models the mean flow and fine-scale turbulent scales with a parabolized Reynolds Averaged Navier-Stokes (RANS) system. The wave components are modeled using a simplified spatial linear stability formulation, which captures the growth and evolution of the coherent structures. Comparisons with the high fidelity Large Eddy Simulations (LES) of the turbine wakes showed that this framework was able to capture the additional wake mixing and faster wake recovery in the far wake regions for both the pulse and helix AWM strategies with minimal
10 computational expense. In the near wake region, some differences are observed in both the RANS velocities profiles and initial growth of the large-scale structures, which may be due to some simplifying assumptions used in the model.

## 1 Introduction

There are several unsteady phenomena that affect large-scale structures in turbine wakes and influence wake dynamics that arise from factors such as atmospheric conditions and turbine control strategies. Existing steady-state models are often inadequate
15 for capturing these complexities, and instead, a reduced-order model that can accurately represent flow instabilities and their impact on the wake's evolution is needed. In this paper, such a model is developed and used to analyze wake recovery in the context of wind farm flow control. However, it is important to note that the insights gained from this modeling approach may also be relevant for modeling other processes, such as wind farm layout optimization.

Wind farm flow control methods are primarily designed to reduce power losses in wind farms due to the effects of wakes
20 on downstream turbines. Common approaches include static or dynamic adjustments to the settings of upstream turbines, such as modifying the induction factor (turbine derating), yaw angle (wake steering), or blade pitch (wake mixing) (Meyers et al., 2022). This work focuses specifically on active wake mixing (AWM), which aims to excite flow instabilities in the wake to enhance the entrainment of mean velocity, resulting in faster wake recovery.

Following Cheung et al. (2024a), AWM can be implemented by specifying a dynamic blade pitch, $\theta(t)$, on top of the baseline
25  pitch set point, $\theta_0(t)$ as,

$$\theta(t) = \theta_0(t) + A\cos(\omega_e t - \kappa_\Theta(\psi(t) + \phi_{\text{clock}})), \qquad (1)$$

where $A$ is the pitching amplitude, $\omega_e$ is the excitation frequency, $\psi$ is the azimuth position of the blade, $\phi_{\text{clock}}$ is the clocking
angle, and $\kappa_\Theta$ is an azimuthal wavenumber. The parameter $\kappa_\Theta$ controls the structure of the flow instabilities imparted on
the wake and is often used to distinguish between different AWM strategies. Examples include the pulse method ($\kappa_\Theta = 0$),
30  which generates an axisymmetric instability in the flow through collective blade pitching (Goit and Meyers, 2015; Munters
and Meyers, 2018), and the helix method ($\kappa_\Theta = -1$), which uses individual pitch control to impart a helical structure on the
wake that rotates in the direction opposite the turbine (Frederik et al., 2020a). The instabilities actuated in the wake according
to an excitation frequency, which can be specified through a Strouhal number based on the inflow velocity, $U_{inf}$, and turbine
diameter, $D$, as $\omega_e = 2\pi St U_{inf}/D$. Strouhal numbers based on the natural unsteady properties of the wake are typically sought
35  ($St \approx 0.3$), leading to flow structures that are generated over much longer periods than a rotor period (Frederik et al., 2020b).

One type of existing reduced-order wake model is the steady-state, analytical one. This type of model finds its roots in the
Jensen (Jensen, 1983) and Ainslie (Ainslie, 1988) models, for instance, and also includes more recent, sophisticated versions
such as the cumulative curl model (Bastankhah and Porté-Agel, 2014). Many researchers and engineers currently interface with
these models through the FLORIS code developed at NREL (Sinner and Fleming, 2024), which is widely used to optimize
40  wind farm performance. The inherently steady-state nature of these models and their reliance on empirical tuning limits their
applicability in scenarios where unsteady flow features are critical. Recent work has shown this is the case for AWM by
connecting the performance of different AWM strategies to the underlying fluid mechanics associated with the induced flow
instabilities, particularly the interactions between unsteady coherent flow structures and wake recovery dynamics (Korb et al.,
2023; Cheung et al., 2024a). Notably, Cheung et al. (2024a) introduced a spatial linear stability analysis to quantify the growth
45  characteristics of initial flow disturbances based on the temporal forcing frequency and forced azimuthal wavenumber, and
showed a correlation between turbulent entrainment statistics in the wake and modal energy gain. These findings suggest that
an accurate model for AWM should be capable of representing the unsteady effects of coherent structures on the flow.

The behavior of large-scale coherent structures in various canonical shear flows is a well-studied problem with a vast body of
existing literature. A number of previous works describe the formation and behavior of these structures in turbulent boundary
50  layers (Hussain, 1986; Robinson et al., 1991), free shear layers (Ho and Huerre, 1984), jets (Crow and Champagne, 1971),
and wakes (Fuchs et al., 1979). Of particular relevance to the current work are the theoretical and modeling approaches used
to analyze such flows. Hussain and Reynolds (1970) introduced the concept of a triple-decomposition analysis to separate the
mean flow, fine-scale turbulent components, and wave components of flow, which was widely used in modeling jet (Iqbal and
Thomas, 2007) and boundary layer (Kwon et al., 2016) flows. A number of previous studies have shown that the growth of the
55  coherent structures in shear flows can be modeled by spatial stability theory (Cheung and Lele, 2009; Cheung and Zaki, 2011),
and noted that the coupling the growth of the large scale structures to the mean flow evolution was critical to capturing the

**Table 1.** Hub-height wind speed conditions used in the turbine wake study. All values are taken from the simulated atmospheric boundary layer.

| Name | Wind-Speed (WS) | Turb. intensity (TI) | Shear Exponent | Rotor disk veer |
|---|---|---|---|---|
| Low WS/Low TI | 6.52 m/s | 0.036 | 0.142 | 7.9° |
| Med WS/Low TI | 9.05 m/s | 0.031 | 0.160 | 8.9° |
| High WS/Low TI | 11.58 m/s | 0.035 | 0.156 | 5.6° |

behavior of the flow. However, these modeling approaches have yet to be applied to the problem of turbine wakes, leading to a large gap between the currently available steady state wake models and computationally expensive, high fidelity simulations.

The objective of the current work is to develop a physics-based, computationally efficient model that can capture the effects of active wake mixing on turbine wakes. While turbine wakes contain significant differences from the canonical jet flows discussed above, we show that by using a triple-decomposition approach, we can still capture the mean flow using a parabolized RANS model, and the large scale structures can be modeled with a spatial linear stability formulation. In the following sections, we describe the mathematical formulation used in this study and the high fidelity numerical simulations of the turbine wakes used to calibrate and evaluate the reduced order model. We then show comparisons between LES calculations and the RANS with linear stability model for different AWM strategies, and conclude with a summary of the work and a discussion of future work in this area.

# 2 Methodology

## 2.1 Atmospheric and turbine conditions of interest

Though the current model is meant to be broadly applicable to all turbine wake flows from both onshore and offshore horizontal axis wind turbines, this work focuses on modeling AWM as applied to larger offshore wind turbines under stable atmospheric conditions. For these modern wind turbines, the application of AWM can potentially lead to substantial wake benefits and noticeable AEP gains. For offshore locations, the prevalence of stably stratified conditions can also lead to many situations where the turbine wakes are especially long and any naturally occurring wake mixing is inhibited.

Representative offshore conditions were selected for this study based on measured data from a floating lidar measurement campaign conducted off the NY bight (Mason, 2022; DNV, 2023). The floating lidar data, collected in 10 minute intervals over a period of 1.6 years, provided velocity and turbulence intensity (TI) profile information for heights between 20m and 200m. From this data, a selection process was undertaken to generate three representative wind speed profiles with relatively low TI (see table 1) as described in Brown et al. (2025).

These conditions corresponded to the likely operating range of the IEA 15MW reference turbine where AWM strategies might be deployed. The IEA 15MW reference turbine was used in this study due to its similarity with current offshore wind

**Table 2.** Details of the IEA15MW reference turbine

| Name | Wind-Speed |
|---|---|
| Hub-height | 150 m |
| Rotor diameter | 240 m |
| Rated wind speed | 10.59 m/s |
| Design Ct | 0.804 |
| Design TSR | 9.0 |

turbines being developed by major turbine OEM's. The details of this turbine are summarized in table 2, with additional information available from Gaertner et al. (2020).

As discussed in section 2.5.1, the selected wind conditions and turbine model were used to set up high-fidelity LES calculations for turbines with and without AWM activated. The LES data was then used to calibrate RANS closure model coefficients in the wake model, and to compare the accuracy of the final outputs from the model.

## 2.2 Mathematical formulation

To model both the steady-state wake profiles and the unsteady dynamics of coherent structures which may be excited through AWM, we use the triple-decomposition approach pioneered by Hussain and Reynolds (1970) in their studies of boundary layer flows. The triple-decomposition formulation separates the flow variables $\mathbf{u}(\mathbf{x},t)$ into the three components

$$\mathbf{u}(\mathbf{x},t) = \overline{\mathbf{U}}(\mathbf{x}) + \langle \mathbf{u}(\mathbf{x},t) \rangle + \mathbf{u}'(\mathbf{x},t). \tag{2}$$

where $\overline{\mathbf{U}}(\mathbf{x})$ is the time-averaged mean flow, $\langle \mathbf{u}(\mathbf{x},\mathbf{t}) \rangle$ is the phase-averaged velocities, and $\mathbf{u}'(\mathbf{x},t)$ are the fine scale turbulent fluctuations. The mathematical operations required to compute the mean flow over an averaging time $T$ is given by

$$\overline{f} = \frac{1}{T} \int_0^T f(\mathbf{x},t) \, \mathrm{d}t \tag{3}$$

and the phase average is given by

$$\langle f \rangle = \frac{1}{N} \sum_{n=0}^{N} f(\mathbf{x},t+n\tau) \tag{4}$$

for a given time period $\tau$ of the coherent structure and for a specified number of periods $N$. Once the mean and the phase averaged velocities are known, the fine scale fluctuating components can be calculated as $\mathbf{u}'(\mathbf{x},t) = \mathbf{u}(\mathbf{x},t) - \overline{\mathbf{U}}(\mathbf{x}) - \langle \mathbf{u}(\mathbf{x},t) \rangle$. The wave component $\tilde{\mathbf{u}}(x,t)$ of the flow field is defined as

$$\tilde{\mathbf{u}}(x,t) = \langle \tilde{\mathbf{u}}(x,t) \rangle - \overline{\mathbf{U}}(\mathbf{x})$$
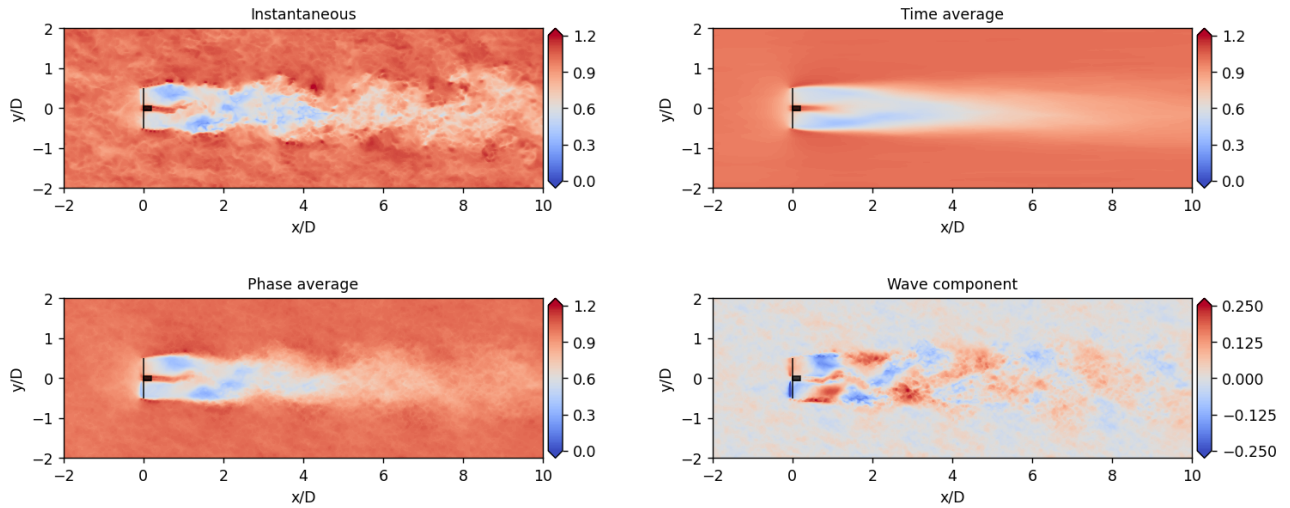
**Figure 1.** An example of a triply decomposed flow field for a wind turbine wake. This case is from the HelixA4 case under stable Low WS/Low TI ABL conditions with $4°$ amplitude forcing. In each contour the normalized streamwise velocity $U/U_\infty$ is plotted.

An example of a turbine wake which has been triply-decomposed is shown in Figure 1. In this case, the turbine flow field was calculated using LES and averaged according to definitions (3) and (4), which leads to clear depictions of the mean flow field features as well as the large-scale coherent structures which develop within the wake.

One advantage of using the triple-decomposition approach is that it allows for computationally efficient models to be developed which can solve for each of the three components. Interactions between the different flow components can also be included which show how the large-scale coherent structures can impact the mean flow and vice-versa. In the following sections, we describe how a parabolic RANS model can be used to efficiently capture the mean flow and fine-scale turbulent flow components. This is coupled to a linear stability model for the wave components of the flow, and we show that as the large scale coherent structures develop within the wake, the mean velocity profiles are impacted as well, leading to the desired wake mixing behavior in this application.

## 2.3 RANS model

In this section, a RANS model is formulated to couple the effects of coherent structures and turbulence on the evolution of the mean velocity field. The model is based on the standard $k$-$\varepsilon$ RANS closure model (Jones and Launder, 1972); however, a few assumptions are made to simplify the model, as the focus is on developing a computationally efficient representation of the effects of active wake mixing on the mean flow. First, the dynamics are assumed to be axisymmetric, reducing the complexity of the model to two-dimensions. Second, the boundary layer approximation is applied so that: (1) second order derivatives in the streamwise direction, $x$, are small relative to those in the radial direction, $r$; (2) the radial pressure gradient is decoupled from the velocity field; and (3) turbulent production is dominated by the radial mean streamwise velocity gradient. This leads

to a parabolic system that can be marched in the downstream direction, as in Cheung et al. (2024b). Lastly, direct interactions
between the coherent structures and the turbulence are neglected so that AWM only forces the evolution of the mean velocity.
The resulting equations are

$$\frac{\partial \bar{U}}{\partial x} + \frac{\partial \bar{V}}{\partial r} + \frac{\bar{V}}{r} = 0 \tag{5a}$$

$$\bar{U}\frac{\partial \bar{U}}{\partial x} + \bar{V}\frac{\partial \bar{U}}{\partial r} = \frac{1}{r}\frac{\partial}{\partial r}\left[r(\nu + \nu_t)\frac{\partial \bar{U}}{\partial r}\right] + F_{\text{CS}} \tag{5b}$$

$$\bar{U}\frac{\partial k}{\partial x} + \bar{V}\frac{\partial k}{\partial r} = \nu_t\left(\frac{\partial \bar{U}}{\partial r}\right)^2 - \varepsilon + \frac{1}{r}\frac{\partial}{\partial r}\left[r(\nu + \nu_t/\sigma_k)\frac{\partial k}{\partial r}\right] \tag{5c}$$

$$\bar{U}\frac{\partial \varepsilon}{\partial x} + \bar{V}\frac{\partial \varepsilon}{\partial r} = \frac{C_{1\varepsilon}\varepsilon}{k}\left[\nu_t\left(\frac{\partial \bar{U}}{\partial r}\right)^2\right] - \frac{C_{2\varepsilon}}{k}\varepsilon^2 + \frac{1}{r}\frac{\partial}{\partial r}\left[r(\nu + \nu_t/\sigma_\varepsilon)\frac{\partial \varepsilon}{\partial r}\right] \tag{5d}$$

where $\bar{U}$ and $\bar{V}$ are the mean streamwise and radial velocity components, respectively. The effects of turbulence, $U'$, on the
mean flow are represented by the eddy-viscosity $\nu_t = C_\mu k^2/\varepsilon$, where $k$ and $\varepsilon$ are the turbulent kinetic energy and dissipation.
To close the $k$-$\varepsilon$ model, the constants are calibrated based on LES data in Section 2.3.1. It is important to note that this model
is not limited to the $k$-$\varepsilon$ turbulence model; rather, it represents one common approach to modeling the effects of turbulence.
The term $F_{\text{CS}}$ represents forcing of the mean flow by the wave component, $\tilde{\mathbf{u}}$

$$F_{\text{CS}} = -\overline{\tilde{u}\frac{\partial \tilde{u}}{\partial x} + \tilde{v}\frac{\partial \tilde{u}}{\partial r}} \tag{6}$$

and the coupling between the mean component and wave component is discussed further in Section 2.4.

To solve equations (5a)-(5d), they are discretized on a uniform grid in the radial direction using a second-order centered
difference method. The radial domain extends to $r_{\max} = 5R$ with a uniform spacing of $\Delta r = 0.025R$. In the $x$-direction, the
equations are discretized around the cell centers and a Crank-Nicolson method is used to march $20D$ downstream with uniform
step sizes of $\Delta x = 0.1R$. The resulting tridiagonal system is solved using an iterative solver, which advances the solution from
one $x$-location to the next.

For each variable, Neumann boundary conditions are applied at $r = 0$,

$$\frac{\partial \bar{U}}{\partial r}(r=0) = 0, \qquad \frac{\partial k}{\partial r}(r=0) = 0, \qquad \frac{\partial \varepsilon}{\partial r}(r=0), \qquad \frac{\partial \bar{V}}{\partial r}(r=0) = 0,$$

and Dirichlet boundary conditions are applied at $r = r_{\max}$,

$$\bar{U}(r=r_{\max}) = U_\infty, \qquad k(r=r_{\max}) = k_\infty, \qquad \varepsilon(r=r_{\max}) = 0,$$

where $k_\infty/U_\infty^2 = 1.0 \times 10^{-3}$ is specified based on the LES calibration data. Note that the continuity relation (5a) only requires
one boundary condition to be imposed on $\bar{V}$.

A hyperbolic tangent profile is used to model the initial condition for $\bar{U}$ at $x = x_0$,

$$\bar{U}(x_0) = 0.5(U_\infty - U_0)\left(1 + \tanh\left(\frac{r - r_e}{\Delta}\right)\right) + U_0, \tag{7}$$

where the nondimensionalized values $U_0/U_\infty = 0.5$, $r_e/R = 1.2$, and $\Delta/R = 0.05$ were determined to provide a good agreement with the azimuthally averaged velocity deficit profiles from the LES data near $x/D = 2$ (see Figures 4 and 5). However, it should be noted that the effects of the nacelle in the near wake are not accounted for in the RANS formulation. The initial profile for $k$ is taken to be proportional to the square of the mean velocity gradient, $k(x_0) \sim (\partial \bar{U}/\partial r)^2 + k_\infty$, such that $\sqrt{3\max(k(x_0))/2} = 0.125$, and the initial $\varepsilon$ is taken to balance turbulent kinetic energy production, i.e., $\varepsilon(x_0) = \sqrt{C_{1\varepsilon}k^2(\partial \bar{U}/\partial r)^2}$.

### 2.3.1 Calibration of RANS

The coefficients $C_\mu, C_{1\varepsilon}, C_{2\varepsilon}$ of the $k - \epsilon$ RANS closure model were calibrated to match the rotor averaged velocities from the baseline LES. Since the RANS formulation does not account for the hub and nacelle region from the LES (see fig. 1), the calibration was formulated to match the rotor averaged velocities from a distance of $x/D = 2.0$ to $x/D = 8.0$. The cost function for this calibration was a $\mathcal{L}_2$ norm error between the RANS output and the LES output. `L-BFGS-B` (Byrd et al., 1995; Zhu et al., 1997) algorithm as implemented in `scipy` was used for the calibration. The optimal values from this calibration are $C_\mu = 0.0035, C_{1\varepsilon} = 0.163, C_{2\varepsilon} = 2.86$. It is important to note that these values are particular to the initial conditions and RANS closure model used, and not a general guideline for wake predictions. It is also to be noted that the calibration is only performed for the baseline cases and not the AWC cases. The constants $\sigma_k$ and $\sigma_\varepsilon$ were not included in the calibration process; instead, the standard values $\sigma_k = 1.0$ and $\sigma_\varepsilon = 1.3$ proposed by Jones and Launder (1972) were used. Figure 7 shows a close match between the baseline RANS and LES results, showing that these calibrated parameters are representative model constants for capturing the wake behavior in the baseline cases, and will be used for all the RANS results presented in this work.

## 2.4 Linear stability model

In this work, we are primarily interested in evaluating the feasibility of using a wave component model to determine the impact of large scale coherent structures on the turbine wakes. Many approaches have been used previously in the literature to capture the dynamics of large scale structures in shear flows, including linear and nonlinear stability analysis (Cheung and Lele, 2009), non-modal stability analysis (Hack and Zaki, 2015), and global stability analysis (Schmid, 2007). These methodologies have been very well developed and successful in analyzing other canonical flows such as pipe flows, boundary layers, and jets.

As an initial step towards demonstrating the feasibility of this modeling approach, a simple parallel flow, inviscid, spatial linear stability analysis was chosen for this work. The focus of the analysis is to model the growth of the large scale coherent structures and capture resulting changes to the mean flow of the turbine wake with minimal computational effort. Additional effects not captured in this analysis, such the effects of shear, veer, swirl, or atmospheric stratification, will be included in future analyses.

### 2.4.1 Piecewise constatnt velocity profile

Analytic solutions to the spatial linear stability problem are possible if we assume the wake turbine profile remains axisymmetric and roughly follows a piecewise constant profile. In the current work, we adopt the two-step profile shown in figure 2, which is defined by

$$\overline{U}_{pw}(r) = \begin{cases} U_0, & r < r_1 \\ U', & r_1 \leq r \leq r_2 \\ U_\infty, & r > r_2 \end{cases} \tag{8}$$

where $U_0$ is the centerline velocity, $U_\infty$ is the freestream velocity, and $U' = \frac{1}{2}(U_0 + U_\infty)$ is the averged velocity of the wake shear region from $r_1 \leq r \leq r_2$. During the solution process, the $r_1$ and $r_2$ parameters can be chosen so that the displacement $\delta$ and momentum $\delta_w$ areas of the $\overline{U}_{pw}$ profile match that same displacement and momentum areas calculated from the RANS mean flow profiles $\overline{U}_{RANS}$. Using the following definitions for $\delta$ and $\delta_\theta$:

$$\delta(\overline{U}) = 2\pi \int\limits_0^\infty \left(1 - \frac{\bar{U}(r)}{U_\infty}\right) r \, \mathrm{d}r \tag{9}$$

$$\delta_\theta(\overline{U}) = 2\pi \int\limits_0^\infty \frac{\bar{U}(r)}{U_\infty} \left(1 - \frac{\bar{U}(r)}{U_\infty}\right) r \, \mathrm{d}r \tag{10}$$

$r_1$ and $r_2$ are then found by solving the following algebraic system:

$$\delta(\overline{U}_{pw}) = \delta(\overline{U}_{RANS}) \tag{11a}$$

$$\delta_\theta(\overline{U}_{pw}) = \delta_\theta(\overline{U}_{RANS}) \tag{11b}$$

An additional simplification is possible if we assume that the wake shear region remains small relative to the size of the rotor diameter. In this case, we can decompose the $\overline{U}_{pw}$ profile into

$$\overline{U}_{pw}(r) = \overline{U}^{(0)}(r) + \overline{U}^{(1)}(r) \tag{12}$$

where $\overline{U}^{(0)}$ is the Heaviside step function

$$\overline{U}^{(0)}(r) = \begin{cases} U_0, & r \leq r_e \\ U_\infty, & r > r_e \end{cases} \tag{13}$$
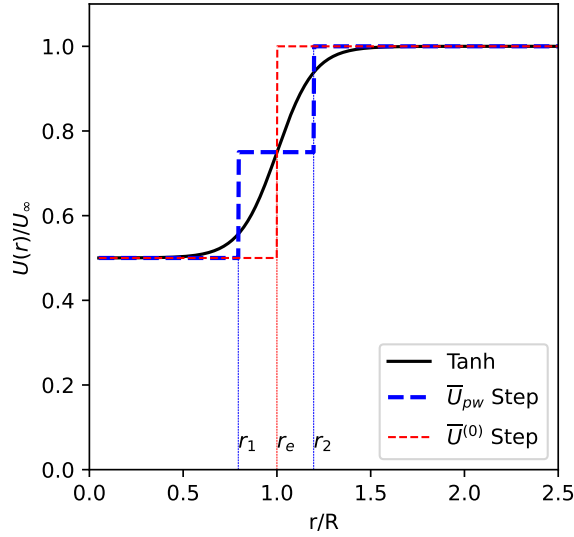
**Figure 2.** Comparison of the step profile with the hyperbolic tangent profile

and $\overline{U}^{(1)}$ is a small perturbation to the single step profile:

$$\overline{U}^{(1)}(r) = \begin{cases} 0, & r < r_1 \\ +\Delta U, & r_1 \leq r \leq r_e \\ -\Delta U, & r_e \leq r \leq r_2 \\ 0, & r > r_2 \end{cases} \tag{14}$$

This assumption allows the analytical results of Batchelor and Gill (1962) to be directly applied with some minor modifications,
195   as discussed in the following section.

### 2.4.2   Spatial linear stability formulation

For the flow variables $\tilde{\phi} = [\tilde{u}\ \tilde{v}\ \tilde{w}\ \tilde{p}]$, we assume that they can be expressed in terms of the radial eigenfunctions $\hat{\phi}_n$ and the complex exponential basis functions

$$\tilde{\phi}(x,r,\theta,t) = \hat{\phi}_n(r)e^{i\alpha x + in\theta - i\omega t}, \tag{15}$$

where $\alpha = \alpha_r + i\alpha_i$ is the complex streamwise wavenumber, $n$ is the azimuthal mode number, and $\omega$ is the temporal frequency. Assuming an inviscid, parallel flow with a piecewise constant velocity profile, the governing equations for mass and momentum conservation of the wave components $\tilde{\phi}$ are

$$\frac{\partial \tilde{u}}{\partial x} + \frac{\partial \tilde{v}}{\partial r} + \frac{\tilde{v}}{r} + \frac{1}{r}\frac{\partial \tilde{w}}{\partial \theta} = 0 \tag{16a}$$

$$\frac{\partial \tilde{u}}{\partial t} + \overline{U}\frac{\partial \tilde{u}}{\partial x} = -\frac{1}{\rho}\frac{\partial \tilde{p}}{\partial x} \tag{16b}$$

$$\frac{\partial \tilde{v}}{\partial t} + \overline{U}\frac{\partial \tilde{v}}{\partial x} = -\frac{1}{\rho}\frac{\partial \tilde{p}}{\partial r} \tag{16c}$$

$$\frac{\partial \tilde{w}}{\partial t} + \overline{U}\frac{\partial \tilde{w}}{\partial x} = -\frac{1}{\rho r}\frac{\partial \tilde{p}}{\partial \theta} \tag{16d}$$

Here $\overline{U}(r) = \overline{U}_{pw}$, with the parameters $r_1$, $r_2$, $U_0$, and $U_\infty$ chosen to match the characteristics of the RANS wake profiles. Inserting the representation (15) in equations (16) leads to the following spectral versions of the governing equations

$$i\alpha \hat{u}_n + \frac{\tilde{v}_n}{r} + \frac{\partial \tilde{v}_n}{\partial r} + \frac{in}{r}\tilde{w}_n = 0 \tag{17a}$$

$$\xi \hat{u}_n + \hat{v}_n \frac{d\overline{U}}{dr} + \hat{f}_n^{(1)} = -i\frac{\alpha}{\rho}\hat{p}_n \tag{17b}$$

$$\xi \hat{v}_n = -\frac{1}{\rho}\frac{d\hat{p}_n}{dr} \tag{17c}$$

$$\xi \hat{w}_n = -i\frac{n}{\rho r}\hat{p}_n \tag{17d}$$

where $\xi(r) = \alpha \bar{U}^{(0)}(r) - \omega$. Note that the $\overline{U}_{pw}$ profile has been decomposed according to equation (12), and the term $\hat{f}_n^{(1)} = i\alpha \overline{U}^{(1)}\hat{u}_n$. Equations (17) can be combined into the Rayleigh ordinary differential equation for the pressure $\hat{p}_n$ variable

$$\frac{1}{r}\frac{d}{dr}\left(r\frac{d\hat{p}_n}{dr}\right) - \left[\left(\frac{n}{r}\right)^2 + \alpha^2\right]\hat{p}_n = i\rho\alpha\hat{f}_n^{(1)}. \tag{18}$$

Both the eigenfunctions $\hat{p}(r)$ and the eigenvalues $\alpha$ can be decomposed into a zeroth order and first order component

$$\hat{p}_n = \hat{p}_n^{(0)} + \hat{p}_n^{(1)} \tag{19a}$$

225 $\quad \alpha = \alpha^{(0)} + \alpha^{(1)}$ (19b)

Here both $\hat{p}_n^{(1)}$ and $\alpha(1)$ are assumed to be small relative to $\hat{p}_n^{(0)}$ and $\alpha(0)$, respectively, and the solution can be found as part of an eigenvalue perturbation problem. Equation (18) can be similarly divided into the zeroth order and first order contributions, where only the appropriate order terms are included in equation:

$$\mathcal{L}\{\hat{p}_n^{(0)}\} = \frac{1}{r}\frac{\mathrm{d}}{\mathrm{d}r}\left(r\frac{\mathrm{d}\hat{p}_n^{(0)}}{\mathrm{d}r}\right) - \left[\left(\frac{n}{r}\right)^2 + \left(\alpha^{(0)}\right)^2\right]\hat{p}_n^{(0)} = 0 \tag{20a}$$

230 $\quad \mathcal{L}\{\hat{p}_n^{(1)}\} + 2\alpha^{(0)}\alpha^{(1)}\hat{p}^{(0)} = i\rho\alpha^{(0)}\hat{f}_n^{(1)}$ (20b)

The zeroth order solution to equation (20a) is given by the modified Bessel functions

$$\hat{p}_n^{(0)}(r) = \begin{cases} C_1 I_n(\alpha^{(0)}r), & r < r_e \\ C_2 K_n(\alpha^{(0)}r), & r \geq r_e \end{cases} \tag{21}$$

The constants $C_1$ and $C_2$ are chosen so the pressure is continuous at $r = r_e$, and the kinematic condition for the displacement $\eta$ of a material line at $r = r_e$ is also satisfied:

235 $\quad \dfrac{\partial\tilde{\eta}}{\partial t} + \overline{U}\dfrac{\partial\tilde{\eta}}{\partial x} = \tilde{v}.$ (22)

Assuming the functional form $\tilde{\eta}(x,\theta,t) = \hat{\eta}e^{i\alpha x + in\theta - i\omega t}$, enforcing above conditions leads to the following nonlinear relation which can be used to solve for $\alpha^{(0)}$ at every frequency $\omega$:

$$\frac{\xi(r_0)^2}{\xi(r_\infty)^2} = \frac{K_n'(\alpha^{(0)}r_e)I_n(\alpha^{(0)}r_e)}{K_n(\alpha^{(0)}r_e)I_n'(\alpha^{(0)}r_e)} \tag{23}$$

Up to this point the analysis follows that of Batchelor and Gill (1962) for piecewise constant velocities, and is shown to be valid for infinitely sharp, top-hat velocity profiles. However, in the current work, capturing the effects of the wake spreading are important to the growth and evolution of large scale structures. This can be accomplished by including a small perturbation to the $\overline{U}^{(0)}$ profile, and calculating the corresponding perturbation to the growth rates. Once $\hat{p}_n^{(0)}$ and $\alpha^{(0)}$ are known, the perturbation $\alpha^{(1)}$ to the wavenumber can be found by applying the inner product

$$\langle f, g \rangle = \int\limits_0^\infty f(r)g(r)\, r\, \mathrm{d}r$$

to equation (20b), leading to

240 $\quad \langle \mathcal{L}\{\hat{p}_n^{(1)}\}, \hat{p}_n^{(0)}\rangle + \langle 2\alpha^{(0)}\alpha^{(1)}\hat{p}^{(0)}, \hat{p}_n^{(0)}\rangle = \langle i\rho\alpha^{(0)}\hat{f}_n^{(1)}, \hat{p}_n^{(0)}\rangle.$ (24)

Because $\hat{p}_n^{(0)}$ is self-adjoint and satifies equation (20a), the terms in equation (24) can be rearranged into the following expression for $\alpha^{(1)}$

$$\alpha^{(1)} = -\frac{(\alpha^{(0)})^2 \int\limits_0^\infty \bar{U}^{(1)} \dfrac{\hat{p}_n^{(0)}\hat{p}_n^{(0)}}{\alpha^{(0)}\overline{U}^{(0)} - \omega} \, r\mathrm{d}r}{2\int\limits_0^\infty \hat{p}_n^{(0)}\hat{p}_n^{(0)} r \, \mathrm{d}r}. \tag{25}$$

The full eigenvalue $\alpha$ can then be reconstructed through equation (19b). The real part of the wavenumber $\alpha_r$ determines the streamwise wavelength of the large scale coherent structures, while the imaginary component $\alpha_i$ dictates the spatial growth of the structures.

To examine the accuracy of this asymptotic, analytic approach with a piecewise constant velocity profile, a comparison of the linear stability solution using a continuous hyperbolic tangent profile (14) and the $\overline{U}_{pw}$ profile from (8) is shown in figure 3. As expected, the dispersion relation $\alpha = \alpha(\omega)$ shows excellent agreement between the approaches when the profile width $\Delta$ is relatively small. For larger values of $\Delta$, the wavenumber $\alpha_r$ calculated using the piecewise constant profile approximation $U_{pw}$ still agreed with the hyperbolic tangent profile, although there were some discrepancies visible for the growth rate $\alpha_i$. However, for the lower frequencies of interest, the agreement between the approaches is still reasonably accurate.

### 2.4.3 Coupled solution process

The spatial linear stability formulation described in section 2.4.2 can be easily integrated into the RANS solution process discussed in section 2.3. At every streamwise location $x$, the RANS velocity profile is first computed assuming $F_{CS} = 0$. This velocity profile is then used in the linear stability formulation to compute the velocity eigenfunctions $\hat{u}$ and $\hat{v}$ and the corresponding wavenumbers $\alpha$. The evolution of the wave component of the flow variables can be calculated using the formula

$$\tilde{u}(x,r,\theta,t) = a_n \hat{u}_n(r) \exp\left(i\int \alpha(x) \, \mathrm{d}x - in\theta - i\omega t\right) \tag{26}$$

where the integral over $\alpha$ in the exponential accounts for the slow changes in growth rate as the mean flow evolves. The initial amplitude of he wave component is given by $a_n$. Once $\tilde{u}$ and $\tilde{v}$ are known, the mean flow correction term $F_{CS}$ can be calculated, and a new RANS velocity profile can be computed for the same $x$ location. This process is repeated until the RANS velocity profiles meet a specified convergence criteria (the Frobenius norm of two successive solutions less than $10^{-7}$), after which the streamwise marching process proceeds to the next location at $x + \Delta x$.

The initial formulation of both the RANS model and the linear stability model was implemented in python and run on workstations with a single CPU for all cases. For typical cases which used 200 grid points in the radial direction and 200 streamwise points, the baseline RANS calculation took 1-2 seconds to compute, and in cases with the RANS model coupled to the linear stability model, the total solve time was approximately 11-12 seconds.
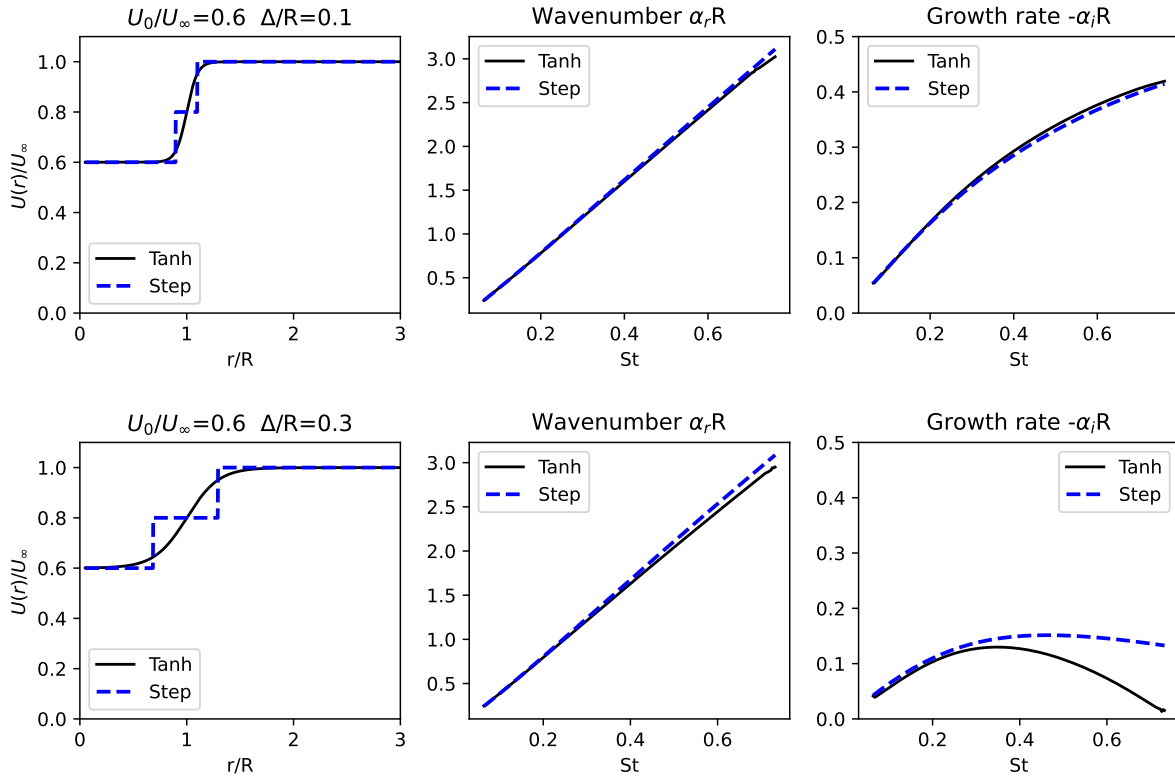
**Figure 3.** Comparison of linear stability theory between the analytic tanh profiles (14) and the piecewise step profiles (8). The first helical mode $n = 1$ is shown in all cases.

## 2.5 AMR-Wind LES calculations

270    To generate the data necessary to calibrate the RANS model coefficients and evaluate the accuracy of the coupled RANS and linear stability approach, a series of large eddy simulations (LESs) of turbine wakes was performed. These were done with the AMR-Wind code (Sharma et al., 2024; Sprague et al., 2020; Mullowney et al., 2021), a massively parallel, block-structured adaptive-mesh, incompressible flow solver for wind turbine and wind farm simulations. AMR-Wind solves the incompressible and low Mach formulations of the Navier-Stokes equations, as well as temperature, subgrid scale kinetic energy, and other 275    scalar equations necessary for LES of wind farms. AMR-Wind solves the discretized equations using a second order finite method and second order temporal integration. AMR-Wind includes all the necessary physics modules to simulate atmospheric boundary layers (ABLs), e.g., mesoscale forcing, Coriolis forcing, geostrophic forcing, Monin-Obukhov similarity theory, gravity forcing, and coupling to OpenFAST (Jonkman et al., 2018; NREL, 2023) for turbine representation using actuator line models.

**Table 3.** AWM parameters

| Name | Modes ($\kappa_\Theta$) | Amplitude ($A$) | Strouhal number ($St$) | Clocking Angle ($\phi_{\text{clock}}$) |
|------|---------|------------------|------------------------|----------------------------------------|
| Baseline | N/A | N/A | N/A | N/A |
| HelixA2 | -1 | 2 deg | 0.30 | 90 deg |
| HelixA4 | -1 | 4 deg | 0.30 | 90 deg |
| PulseA2 | 0 | 2 deg | 0.30 | 90 deg |
| PulseA4 | 0 | 4 deg | 0.30 | 90 deg |

### 2.5.1 Turbine simulation parameters and AWM settings

Simulations using the IEA 15MW reference turbine and the atmospheric conditions listed in section 2.1 were performed in AMR-Wind using the one equation $k_{sgs}$ LES model (Moeng, 1984) and an actuator line model coupled to OpenFAST to represent the turbine blade forces. The simulation domains were either 4.5 km × 2 km × 1 km (Med WS case), or 6.7 km × 2 km × 1 km (Low WS and High WS case). In all cases a background mesh resolution of 5 m was used, which was refined to a resolution of 2.5 m in region 4.75D upstream and 12D downstream of the rotor, leading to mesh sizes of 179M and 309M, respectively. A timestep of 0.02 seconds was used in the turbine simulations, and all simulations had a total runtime of at least 1000 seconds to allow the initial transients to dissipate and the wake structures to fully develop in the flow.

In the baseline turbine simulations, no AWM strategy was employed and the wake was allowed to develop naturally. These baseline cases were compared to simulations where the helix and pulse AWM strategies were used (table 3). All AWM strategies used a single actuation frequency of $St = 0.30$, which is consistent with the Strouhal forcing used in previous studies (Cheung et al., 2024a). The blade pitch amplitudes were set to either 2 degrees or 4 degrees in both the helix and the pulse AWM strategies in order to determine the relative effectiveness of each actuation strategy.

## 3 Results

To evaluate the accuracy of the RANS and linear stability wake model, we compare the modeled wake behavior with the corresponding wake behavior from the AMR-Wind simulations. Results are shown first for the baseline cases where no AWM strategy was used, which allow us to evaluate the underlying RANS model without any coupling to the linear stability model. This is followed by a discussion of the AWM cases with helix and pulse actuation and an evaluation of the full RANS plus linear stability model.

### 3.1 Baseline wake behavior

A comparison of the hub-height velocity profiles between the RANS model and the AMR-Wind LES calculation for the Med WS/Low TI and High WS/Low TI cases is shown in figures 4 and 5, respectively, for various downstream distances. We
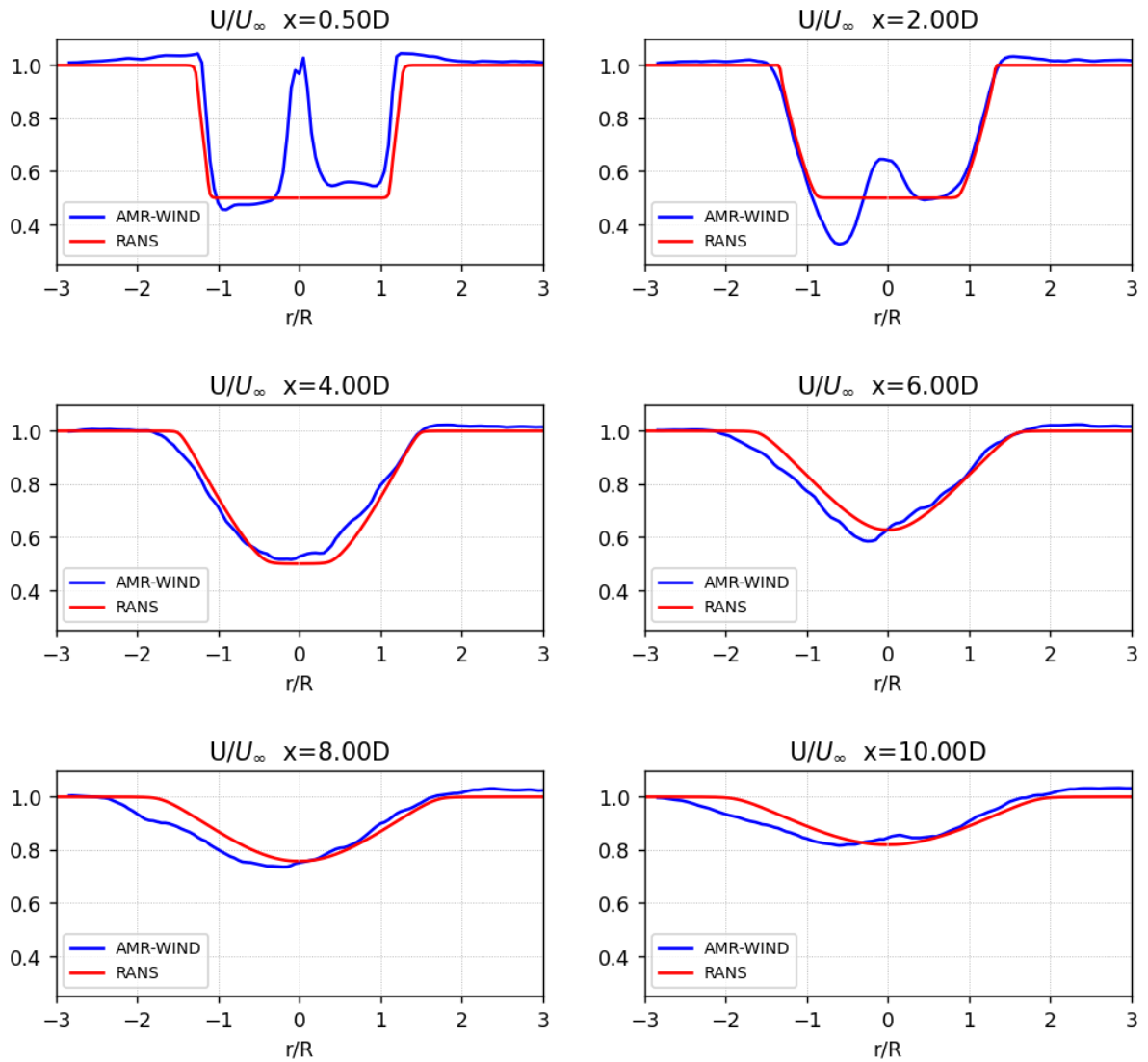
**Figure 4.** Comparison of the normalized hub-height velocity profile between the RANS model and AMR-Wind calculations for the baseline Med WS/Low TI case.

observed that the baseline wake behavior for the Low WS case was very similar to the Med WS case because the turbine was operating at the same thrust coefficient, so the Low WS comparisons are not shown below for the sake of brevity.

In the medium to far wake regions, for downstream distances $x/D > 3.0$, good agreement is seen for the wake profiles from
305 the RANS model and the AMR-Wind calculations. The general evolution of the wake deficit and the wake spreading behavior is well captured by the parabolized RANS model. The AMR-Wind wake profiles show evidence of veer effects, which causes
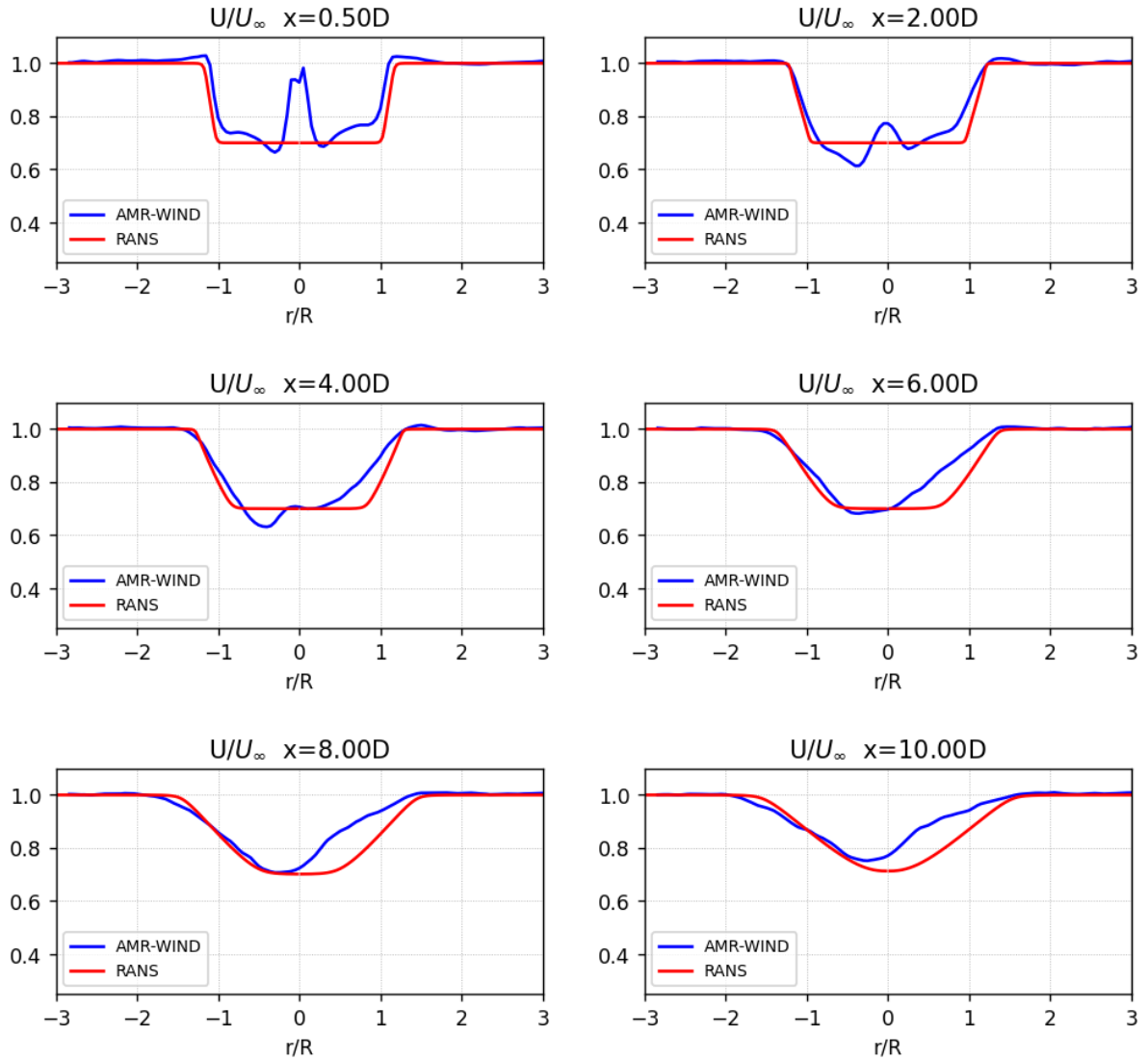
**Figure 5.** Comparison of the normalized hub-height velocity profile between the RANS model and AMR-Wind calculations for the baseline High WS/Low TI case.

asymmetry in the LES wake profiles. This effect is not captured by the RANS model due to the axisymmetric formulation, but the overall match between the methods remains high.

Very close to the turbine rotor some differences between the wake profiles are noticeable. For streamwise distances $x/D < 3.0$ we see the influence of the hub and nacelle on LES wake profiles which is not captured in the RANS model. The actuator line representation of the turbine in AMR-Wind more accurately models the aerodynamics near the hub and root sections of the
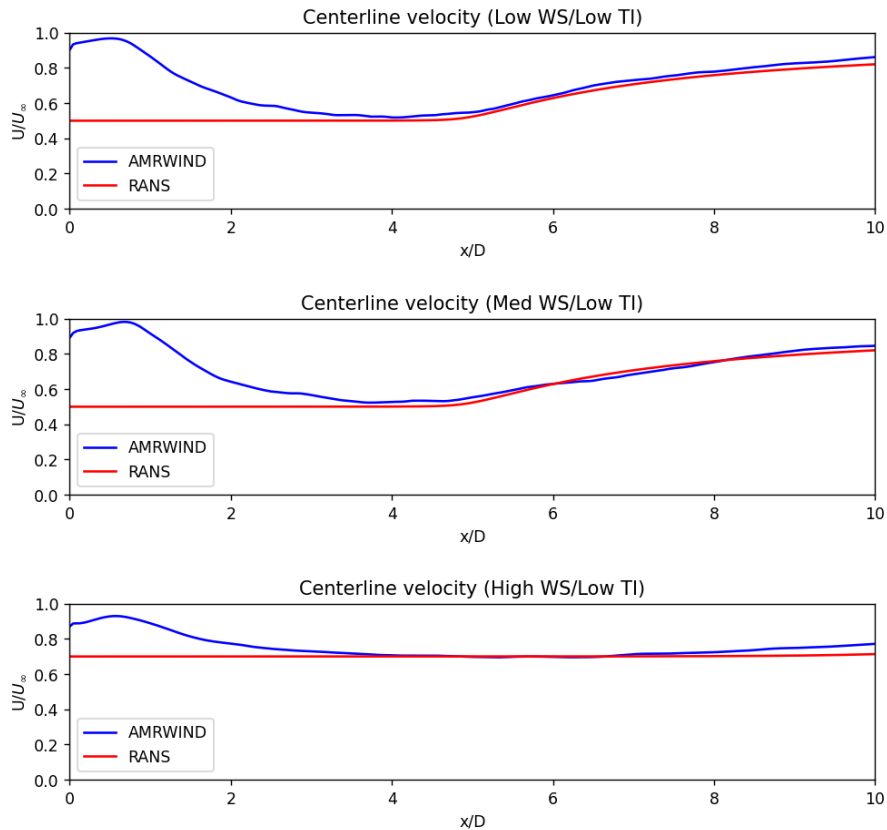
**Figure 6.** Comparison of the normalized centerline velocity profiles for the baseline turbine wakes without AWM.

blade, leading to small recirculation zone immediately downstream of the nacelle. The simplified nature of the initial RANS profiles neglects these effects, as well as any asymmetries due to the interactions of swirl with shear and veer in addition to speedup of the ambient flow from wake blockage. However, despite these approximations, the RANS model still accurately

315 captures the velocity shear near the wake edges.

A comparison of the centerline and rotor averaged velocities shown in figures 6 and 7 provides a similar picture of the RANS model's accuracy for the baseline wake cases. In the far wake region, the RANS model accurately predicts the recovery of the centerline and rotor averaged velocities. Very close to the rotor, the RANS model assumes the presence of a potential core region in the wake which is not realistic, so it is unsurprising that the centerline velocities do not agree until $x/D \approx 4.0$.

320 ## 3.2 Comparisons for AWM cases

With the application of an AWM strategy, we expect the turbine wake to mix faster due to the presence of the large scale coherent structures. As shown in figures 8 and 9, the hub-height velocity profiles for the LES calculations and the RANS with linear stability model indicate a faster wake recovery and increased mixing occurring in the downstream wake. For the
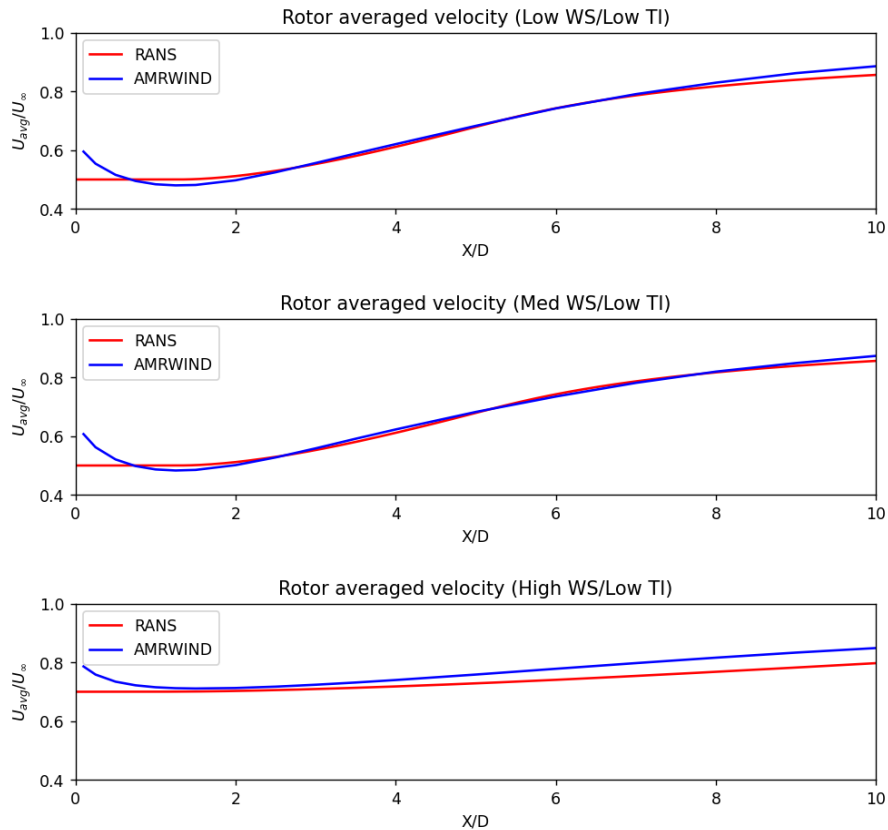
**Figure 7.** Comparison of the normalized rotor averaged velocity profiles for the baseline turbine wakes without AWM.

Med WS/Low TI case in figure 8, there was qualitative agreement between the LES calculations and RANS with linear stability
325   model in predicting the changes to the wake width and centerline velocity changes, for both the helix and pulse AWM cases, and
for both 2° and 4° pitch actuation. For the helix AWM case at the High WS/Low TI condition (figure 9), the LES calculations
show more impact to the centerline velocity recovery, although the RANS with linear stability model still show the changes to
the wake width due to the AWM.

The rotor averaged velocity comparisons in figures 10 and 11 show a similar level of agreement for the AMR-Wind and
330   RANS with linear stability model in the far wake. For downstream distances $x/D > 5.0$, the RANS with linear stability model
qualitatively captured the wake recovery benefits for both the helix and pulse approach. For the High WS/Low TI condition,
it was also seen that the helix AWM was not as effective as in the Med WS/low TI case. This is attributed to the fact that
the turbine operates at a lower thrust coefficient at the higher wind speeds, resulting in less initial wake deficit and lower
velocity shear near the wake edges. The lower shear in the turbine wake translates to slower growth of the large scale coherent
335   structures, meaning that there is less opportunity for them to mix the turbine wake and impact the flow.
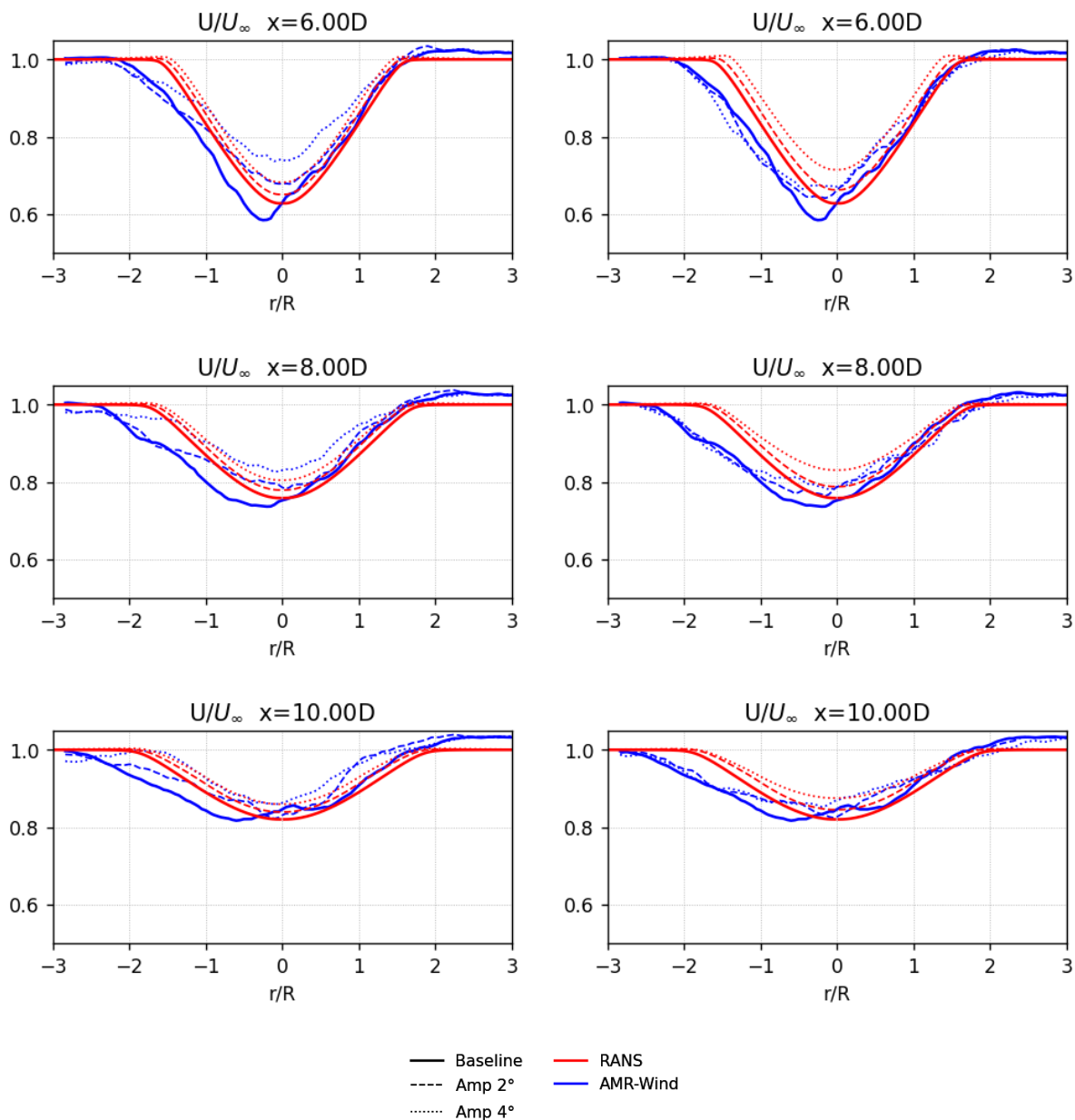
**Figure 8.** Comparison of the hub height velocity profiles for the AMR-Wind and RANS with linear stability model for the Med WS/Low TI case with Helix AWM (right column) and Pulse AWM (left column) actuated.

Some differences between the LES calculations and the RANS with linear stability model are observed in the near wake region of turbine wake. For the Low WS/Low TI and the Med WS/Low TI cases, the growth of the coherent structures in the LES calculations is faster than the RANS with linear stability model, so the wake benefits to the rotor averaged velocity also
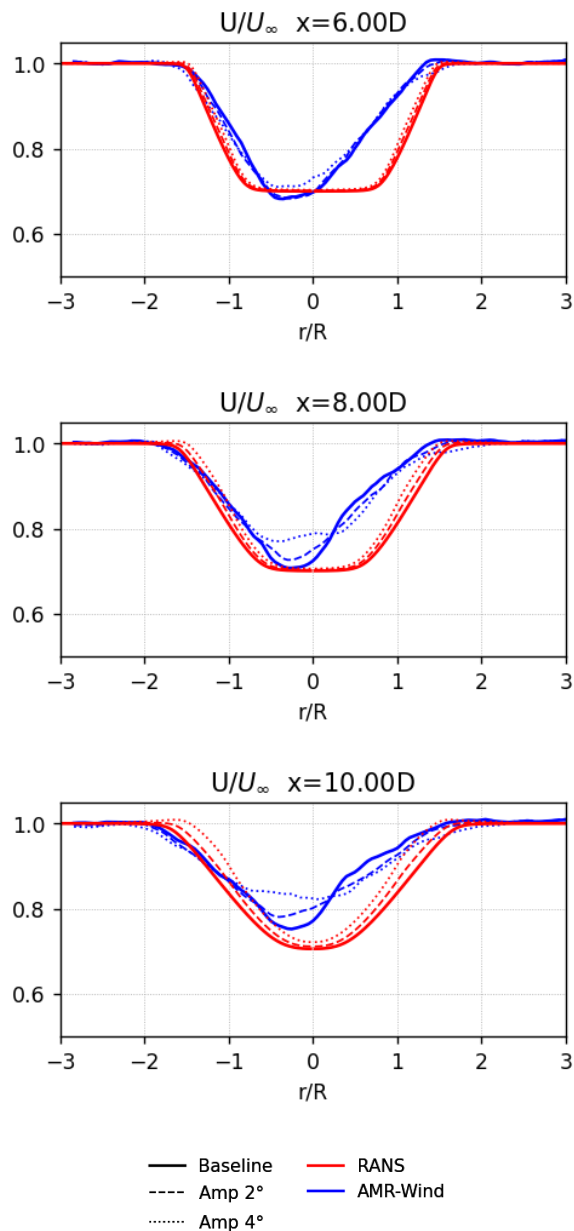
**Figure 9.** Comparison of the hub height velocity profiles for the AMR-Wind and RANS with linear stability model for the High WS/Low TI case with Helix AWM.

appear earlier in the flow. However, in both the LES and the RANS with linear stability model, the growth of the large scale
340   structures saturate at similar levels downstream, so the final wake benefits in the far wake remain comparable.
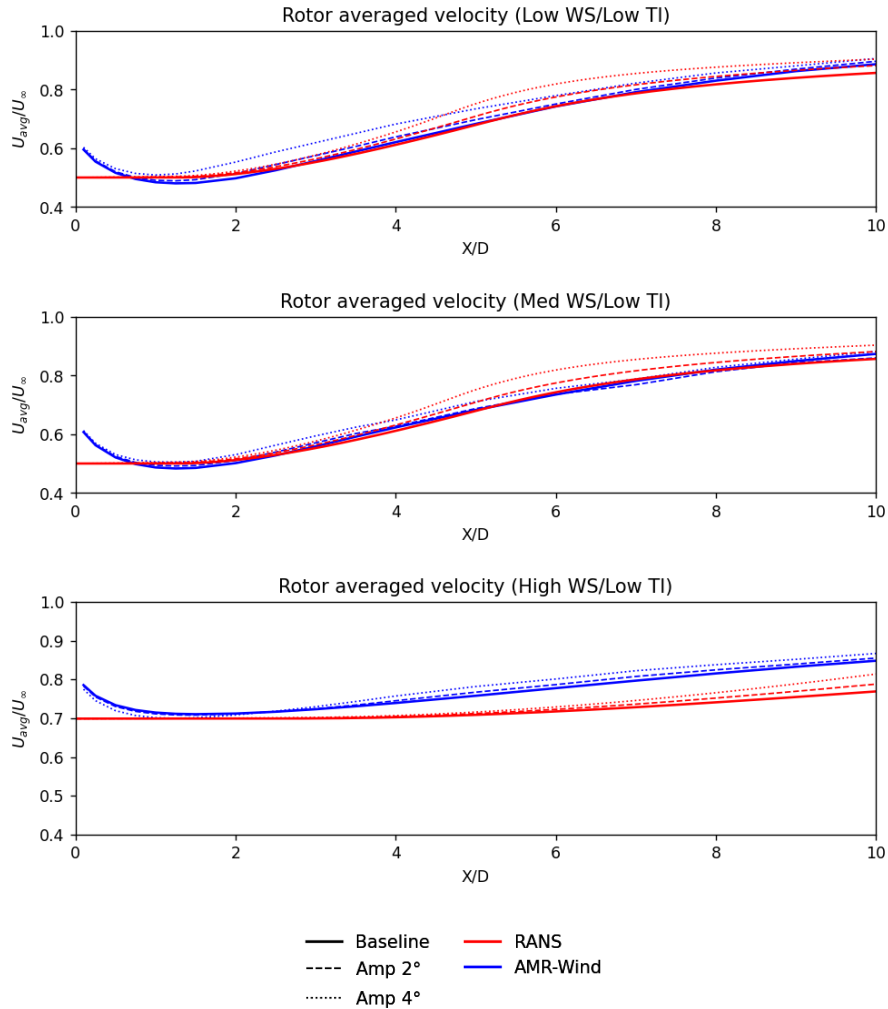
**Figure 10.** Comparison of the normalized rotor averaged velocity profiles for the Low WS, Med WS, and High WS cases using the helix AWM strategy with 2° and 4° actuation amplitudes.

### 3.2.1 Phase averaged velocity

Some insight to the behavior of the large scale structures can be seen in figure 12, where contours of the mean and phase averaged velocity fields is shown for the Low WS/Low TI case. As expected, the near wake region of the RANS and linear stability model fails to capture some flow features immediately downstream of the rotor disk. However, in the far wake region, the differences in the coherent structures between the pulse AWM forcing and the helix AWM forcing become apparent. The wave components in the pulse case form axisymmetric structures with a wavelength of approximately 2D, while a spiral pattern appears in the helix AWC cases with similar wavelength. In the AMR-Wind simulations the structures emerge earlier in the

345
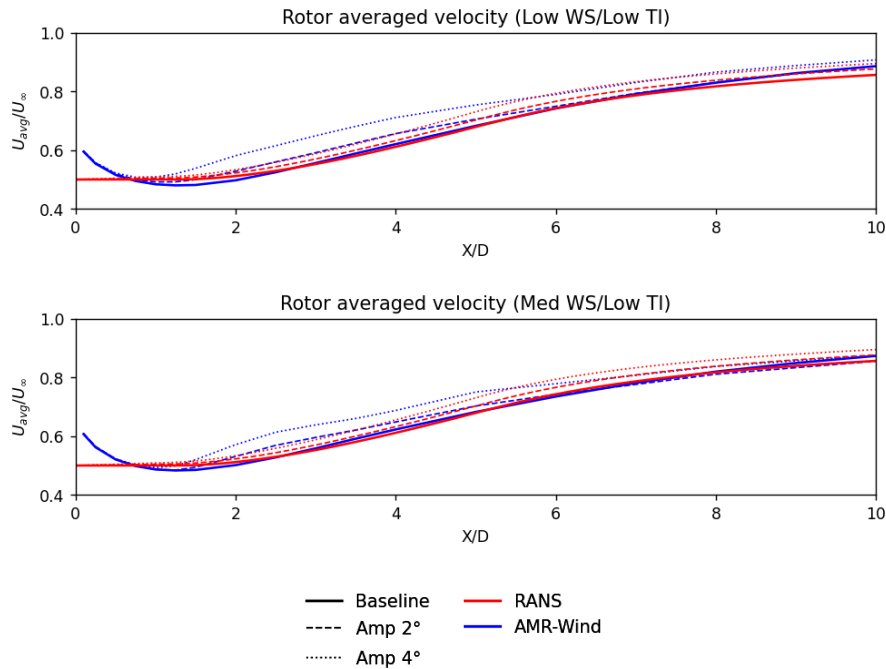
**Figure 11.** Comparison of the normalized rotor averaged velocity profiles for the Low WS and Med WS cases using the pulse AWM strategy with $2°$ and $4°$ actuation amplitudes.

turbine wake, but eventually saturate and impact the wake in a qualitatively similar way compared to the RANS and linear stability model predictions.

## 4 Conclusions

In this work, a framework for modeling AWM was developed that accounts for the effects of both the large-scale coherent structures and the turbulence on the mean flow. Using a triple-decomposition approach, the turbine wake flow was separated into a time-averaged mean flow, fine scale turbulent, and phase averaged components, and a computationally efficient method for solving these components was formulated. An axisymmetric, parabolized $k - \varepsilon$ RANS model was used to solve for the mean flow and fine scale turbulence components. To model the wave components of the flow, a simplified inviscid, parallel-flow, linear spatial stability analysis was used. The linear stability modes were coupled with the RANS model to capture the interactions between the coherent structures and the mean flow.

Comparisons between the RANS with linear stability model and high-fidelity LES calculations of the turbine wakes showed that this framework was able to capture the wake modifications due to AWM actuation, particularly in the far wake regions. Additional wake mixing and more rapid wake recovery was observed for both the pulse and helix AWM strategies. Some differences are also observed in the near wake region of the flow. The high-fidelity LES calculations include non-axisymmetric
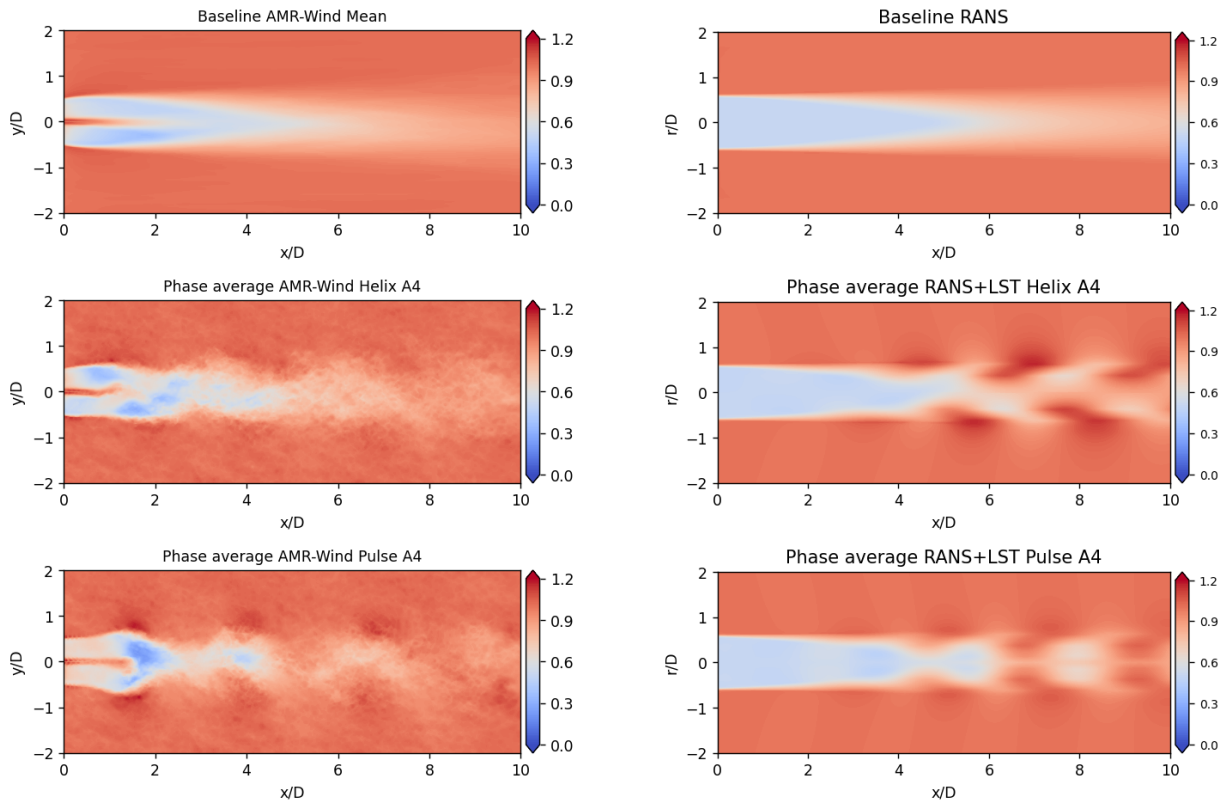
**Figure 12.** Comparison of the AMR-Wind and RANS with linear stability mean velocity component (top row) with the phase averaged velocity for the HelixA4 (middle row) and PulseA4 (bottom row) cases. In all cases the normalized streamwise velocity $U/U_\infty$ is plotted for the Low WS/Low TI case.

features immediately downstream of the rotor which the baseline RANS model fails to capture, and the impact of the large scale coherent structures is also more evident in the near wake region of the LES cases.

There are several limitations associated with the current formulation of the RANS model that could be improved in future
365 studies. One significant constraint is the axisymmetric assumption, which restricts the model's applicability in realistic environments, such as ABLs characterized by large veer. To address this limitation, a parabolic three-dimensional version of the model could be developed using the same principles established here by marching two-dimensional wake profiles downstream, similar to the improvements suggested by Cheung et al. (2024b). Furthermore, incorporating direct interactions between the coherent flow structures and the turbulence may resulting in a more accurate representation of the flow dynamics, although the
370 effect on the mean flow from these higher order interactions remains unknown. Lastly, this work has demonstrated the importance of calibrating the RANS model constants; however, further work is needed to establish robust values for these constants, including the use of additional data in the calibration process.

Additional improvements to the linear stability model are also possible. The current model ignores the effects of swirl, shear, and veer, which impacts the growth of the coherent structures and can help improve the comparisons with the high fidelity simulations. It may also be possible to use the full RANS velocity profile in the Rayleigh equation, instead of a piecewise constant approximation, which would help improve near wake predictions. Finally, future work may also investigate the impact of mode-to-mode interactions in a nonlinear stability framework. For example, the interactions between the axisymmetric modes and helical modes may be crucial in determining the optimal forcing strategy, and could be worth exploring in later studies.

*Code and data availability.* The code and data used in this study can be made available upon reasonable request.

*Author contributions.* L. Cheung was responsible for developing the mathematical formulation, model implementation, and manuscript preparation. G. R. Yalla was responsible for the formulation of the reduced order RANS model, model implementation, generation of LES data, and manuscript preparations. M. T. Henry de Frahan was responsible for performance optimization of the RANS model solver, discussions surrounding the AMR-Wind solver, and manuscript contributions. K. Brown was responsible for conceptualization, performing portions of the LES, and manuscript review. P. Mohan was responsible for calibration of the RANS model coefficients, performance optimization of the RANS model solver, and manuscript contributions. A. Hsieh assisted with data post-processing and comparing results. N. deVelder was responsible for the formulation and development of the RANS model. D. Houck assisted with the problem formulation, manuscript review and preparations.

*Competing interests.* The authors declare that they have no conflict of interest.

*Acknowledgements.* Sandia National Laboratories is a multimission laboratory managed and operated by National Technology & Engineering Solutions of Sandia, LLC, a wholly owned subsidiary of Honeywell International Inc., for the U.S. Department of Energy's National Nuclear Security Administration under contract DE-NA0003525.

This work was authored in part by the National Renewable Energy Laboratory, operated by Alliance for Sustainable Energy, LLC, for the U.S. Department of Energy (DOE) under Contract No. DE-AC36-08GO28308. This research used resources of the Oak Ridge Leadership Computing Facility at the Oak Ridge National Laboratory, which is supported by the Office of Science of the U.S. Department of Energy under Contract No. DE-AC05-00OR22725.

This research has been supported in part by the Wind Energy Technologies Office within the Office of Energy Efficiency and Renewable Energy. The views expressed in the article do not necessarily represent the views of the U.S. DOE or the U.S. Government. This written work is authored by an employee of NTESS. The employee, not NTESS, owns the right, title and interest in and to the written work and is responsible for its contents. Any subjective views or opinions that might be expressed in the written work do not necessarily represent the views of the U.S. Government. The publisher acknowledges that the U.S. Government retains a non-exclusive, paid-up, irrevocable, world-wide license to publish or reproduce the published form of this written work or allow others to do so, for U.S. Government purposes. The DOE will provide public access to results of federally sponsored research in accordance with the DOE Public Access Plan.

# References

405  Ainslie, J. F.: Calculating the flowfield in the wake of wind turbines, Journal of wind engineering and Industrial Aerodynamics, 27, 213–224, 1988.

Bastankhah, M. and Porté-Agel, F.: A new analytical model for wind-turbine wakes, Renewable energy, 70, 116–123, 2014.

Batchelor, G. and Gill, A.: Analysis of the stability of axisymmetric jets, Journal of Fluid Mechanics, 14, 529–551, 1962.

Brown, K., Yalla, G., Cheung, L., Houck, D., deVelder, N., Frederik, J., Simley, E., and Fleming, P.: Comparison of wind farm control
410  strategies under a range of realistic wind conditions: wake quantities of interest, 2025.

Byrd, R. H., Lu, P., Nocedal, J., and Zhu, C.: A limited memory algorithm for bound constrained optimization, SIAM Journal on scientific computing, 16, 1190–1208, 1995.

Cheung, L., Brown, K., Houck, D., and deVelder, N.: Fluid-Dynamic Mechanisms Underlying Wind Turbine Wake Control with Strouhal-Timed Actuation, Energies, 17, 2024a.

415  Cheung, L., Yalla, G., Brown, K., , deVelder, N., Houck, D., Herges, T., Maniaci, D., Sakievich, P., and Abraham, A.: Modification of wind turbine wakes by large-scale convective atmospheric boundary layer structures, Journal of Renewable Sustainable Energy, 16, https://doi.org/10.1063/5.0211722, 2024b.

Cheung, L. C. and Lele, S. K.: Linear and nonlinear processes in two-dimensional mixing layer dynamics and sound radiation, Journal of Fluid Mechanics, 625, 321–351, 2009.

420  Cheung, L. C. and Zaki, T. A.: A nonlinear PSE method for two-fluid shear flows with complex interfacial topology, Journal of Computational Physics, 230, 6756–6777, 2011.

Crow, S. C. and Champagne, F.: Orderly structure in jet turbulence, Journal of fluid mechanics, 48, 547–591, 1971.

DNV: NYSERDA Floating LiDAR Buoy Data, https://oswbuoysny.resourcepanorama.dnv.com/download/f67d14ad-07ab-4652-16d2-08d71f257da1, accesssed: 2023-09-30, 2023.

425  Frederik, J. A., Doekemeijer, B. M., Mulders, S. P., and van Wingerden, J.-W.: The helix approach: Using dynamic individual pitch control to enhance wake mixing in wind farms, Wind Energy, 23, 1739–1751, 2020a.

Frederik, J. A., Weber, R., Cacciola, S., Campagnolo, F., Croce, A., Bottasso, C., and van Wingerden, J.-W.: Periodic dynamic induction control of wind farms: proving the potential in simulations and wind tunnel experiments, Wind Energy Science, 5, 245–257, 2020b.

Fuchs, H. V., Mercker, E., and Michel, U.: Large-scale coherent structures in the wake of axisymmetric bodies, Journal of Fluid Mechanics,
430  93, 185–207, 1979.

Gaertner, E., Rinker, J., Sethuraman, L., Zahle, F., Anderson, B., Barter, G. E., Abbas, N. J., Meng, F., Bortolotti, P., Skrzypinski, W., et al.: IEA wind TCP task 37: definition of the IEA 15-megawatt offshore reference wind turbine, Tech. rep., National Renewable Energy Laboratory (NREL), Golden, CO (United States), 2020.

Goit, J. P. and Meyers, J.: Optimal control of energy extraction in wind-farm boundary layers, Journal of Fluid Mechanics, 768, 5–50, 2015.

435  Hack, M. P. and Zaki, T. A.: Modal and non-modal stability of boundary layers forced by spanwise wall oscillations, Journal of Fluid Mechanics, 778, 389–427, 2015.

Ho, C.-M. and Huerre, P.: Perturbed free shear layers, Annual review of fluid mechanics, 16, 365–424, 1984.

Hussain, A. and Reynolds, W.: The mechanics of an organized wave in turbulent shear flow, Journal of Fluid Mechanics, 41, 241–258, 1970.

Hussain, A. F.: Coherent structures and turbulence, Journal of Fluid Mechanics, 173, 303–356, 1986.

440 Iqbal, M. and Thomas, F.: Coherent structure in a turbulent jet via a vector implementation of the proper orthogonal decomposition, Journal of Fluid Mechanics, 571, 281–326, 2007.

Jensen, N. O.: A note on wind generator interaction, Risø National Laboratory, 1983.

Jones, W. P. and Launder, B. E.: The prediction of laminarization with a two-equation model of turbulence, International journal of heat and mass transfer, 15, 301–314, 1972.

445 Jonkman, J. M., Wright, A. D., Hayman, G. J., and Robertson, A. N.: Full-system linearization for floating offshore wind turbines in OpenFAST, in: International Conference on Offshore Mechanics and Arctic Engineering, vol. 51975, p. V001T01A028, American Society of Mechanical Engineers, 2018.

Korb, H., Asmuth, H., and Ivanell, S.: The characteristics of helically deflected wind turbine wakes, Journal of Fluid Mechanics, 965, A2, 2023.

450 Kwon, Y., Hutchins, N., and Monty, J.: On the use of the Reynolds decomposition in the intermittent region of turbulent boundary layers, Journal of Fluid Mechanics, 794, 5–16, 2016.

Mason, J.: Energy Assessment Report, Tech. Rep. 10124962, DNV, 2022.

Meyers, J., Bottasso, C., Dykes, K., Fleming, P., Gebraad, P., Giebel, G., Göçmen, T., and Van Wingerden, J.-W.: Wind farm flow control: prospects and challenges, Wind Energy Science Discussions, 2022, 1–56, 2022.

455 Moeng, C.-H.: A large-eddy-simulation model for the study of planetary boundary-layer turbulence, Journal of the Atmospheric Sciences, 41, 2052–2062, 1984.

Mullowney, P., Li, R., Thomas, S., Ananthan, S., Sharma, A., Rood, J. S., Williams, A. B., and Sprague, M. A.: Preparing an incompressible-flow fluid dynamics code for exascale-class wind energy simulations, in: Proceedings of the international conference for high performance computing, networking, storage and analysis, pp. 1–16, 2021.

460 Munters, W. and Meyers, J.: Towards practical dynamic induction control of wind farms: analysis of optimally controlled wind-farm boundary layers and sinusoidal induction control of first-row turbines, Wind Energy Science, 3, 409–425, 2018.

NREL: OpenFAST Documentation, https://openfast.readthedocs.io, 2023.

Robinson, S. et al.: Coherent motions in the turbulent boundary layer, Annual review of fluid mechanics, 23, 601–639, 1991.

Schmid, P. J.: Nonmodal stability theory, Annu. Rev. Fluid Mech., 39, 129–162, 2007.

465 Sharma, A., Brazell, M. J., Vijayakumar, G., Ananthan, S., Cheung, L., deVelder, N., Henry de Frahan, M. T., Matula, N., Mullowney, P., Rood, J., Sakievich, P., Almgren, A., Crozier, P. S., and Sprague, M.: ExaWind: Open-source CFD for hybrid-RANS/LES geometry-resolved wind turbine simulations in atmospheric flows, Wind Energy, 27, 225–257, https://doi.org/https://doi.org/10.1002/we.2886, 2024.

Sinner, M. and Fleming, P.: Robust wind farm layout optimization, in: Journal of Physics: Conference Series, vol. 2767, p. 032036, IOP Publishing, 2024.

470 Sprague, M. A., Ananthan, S., Vijayakumar, G., and Robinson, M.: ExaWind: A multifidelity modeling and simulation environment for wind energy, in: Journal of Physics: Conference Series, vol. 1452, p. 012071, IOP Publishing, 2020.

Zhu, C., Byrd, R. H., Lu, P., and Nocedal, J.: Algorithm 778: L-BFGS-B: Fortran subroutines for large-scale bound-constrained optimization, ACM Transactions on mathematical software (TOMS), 23, 550–560, 1997.